# Nanomagnetic encoding of shape-morphing micromachines

https://doi.org/10.1038/s41586-019-1713-2

Received: 25 April 2019

Accepted: 4 September 2019

Published online: 6 November 2019

There are amendments to this paper

Jizhai Cui[1,2,4*], Tian-Yun Huang[3,4*], Zhaochu Luo[1,2], Paolo Testa[1,2], Hongri Gu[3], Xiang-Zhong Chen[3], Bradley J. Nelson[3] & Laura J. Heyderman[1,2]

Shape-morphing systems, which can perform complex tasks through morphological transformations, are of great interest for future applications in minimally invasive medicine[1,2], soft robotics[3–6], active metamaterials[7] and smart surfaces[8]. With current fabrication methods, shape-morphing configurations have been embedded into structural design by, for example, spatial distribution of heterogeneous materials[9–14], which cannot be altered once fabricated. The systems are therefore restricted to a single type of transformation that is predetermined by their geometry. Here we develop a strategy to encode multiple shape-morphing instructions into a micromachine by programming the magnetic configurations of arrays of single-domain nanomagnets on connected panels. This programming is achieved by applying a specific sequence of magnetic fields to nanomagnets with suitably tailored switching fields, and results in specific shape transformations of the customized micromachines under an applied magnetic field. Using this concept, we have built an assembly of modular units that can be programmed to morph into letters of the alphabet, and we have constructed a microscale 'bird' capable of complex behaviours, including 'flapping', 'hovering', 'turning' and 'side-slipping'. This establishes a route for the creation of future intelligent microsystems that are reconfigurable and reprogrammable in situ, and that can therefore adapt to complex situations.

It has been a long-standing goal to create intelligent machines that are untethered and can execute tasks at small scales. Magnetic actuation is of particular interest for the control of these machines, because it comes with the advantage of being able to perform tasks in confined and enclosed spaces[15]. In magnetic shape-morphing systems, a mechanical torque is generated when the magnetization of a magnetic medium is not in line with the applied magnetic field[16]. Previous programming of the magnetic configurations could be achieved by reorienting permanent-magnet microparticles in millimetre-sized devices[10,17,18]. For micrometre-sized devices, programming methods such as aligning superparamagnetic nanoparticles[12,19] (region i in Fig. 1a) and selective coating with soft magnetic thin films[20] (region iii in Fig. 1a) have been demonstrated. In this work, we used stadium-shaped single-domain nanomagnets to encode shape-morphing information into micromachines. The use of nanomagnets with lateral dimensions in an intermediate range, between 100 nm and 500 nm (region ii in Fig. 1a), means they are single domain with a stable remanent magnetization and have a tunable magnetic anisotropy at room temperature[21,22]. As a result of the magnetic shape anisotropy, the magnetization is parallel to the long axis of the magnets, pointing in one of the two directions. By implementing arrays of these nanomagnets in a micromachine, the magnetic configuration can be remotely programmed by applying a sequence of magnetizing fields to store the shape-morphing information.

Inspired by origami[23], the art of paper folding, the micromachine is designed with two types of component: rigid panels, some of which are made functional with arrays of single-domain nanomagnets covering the panel surface; and structured 'soft' spring hinges as the connecting creases. In the micromachine design shown in Fig. 1b, there are four panels patterned with 60-nm-thick nanomagnets that can be remotely encoded and manipulated, and one central passive panel (see Extended Data Fig. 1 for a scanning electron microscopy, SEM, image). Arrays of nanomagnets with different magnetic switching fields are fabricated on opposite panels—for example, panels I and II in Fig. 1b. The switching fields of the nanomagnets were engineered by varying the aspect ratios of the nanomagnets while maintaining the same volume (see Methods section 'Nanomagnet design and coercivity' and Extended Data Fig. 2). As given by the magnetic hysteresis loops in Fig. 1c (see Methods section 'Magnetic characterization and encoding'), the coercive fields $B_c$ required to switch the magnets range from about 30 mT for low-aspect-ratio 'wide' nanomagnets (300 nm × 110 nm, nanomagnet type IV), to about 140 mT for high-aspect-ratio 'narrow' nanomagnets (520 nm × 60 nm, nanomagnet type I). The square shape of the loops indicates that they are fully magnetized at remanence. Arrays of type I and type II nanomagnets are patterned on the opposite panels of the four-panel micromachine, and have switching fields of $B_c(\mathrm{I}) \approx 140$ mT and $B_c(\mathrm{II}) \approx 90$ mT, respectively. Type III and type IV nanomagnets with $B_c(\mathrm{III}) \approx 70$ mT and $B_c(\mathrm{IV}) \approx 30$ mT are employed later in this work.

[1]Laboratory for Mesoscopic Systems, Department of Materials, ETH Zurich, Zurich, Switzerland. [2]Laboratory for Multiscale Materials Experiments, Paul Scherrer Institute, Villigen, Switzerland. [3]Institute of Robotics and Intelligent Systems, ETH Zurich, Zurich, Switzerland. [4]These authors contributed equally: Jizhai Cui, Tian-Yun Huang. *e-mail: huangt@ethz.ch; jizhai.cui@psi.ch

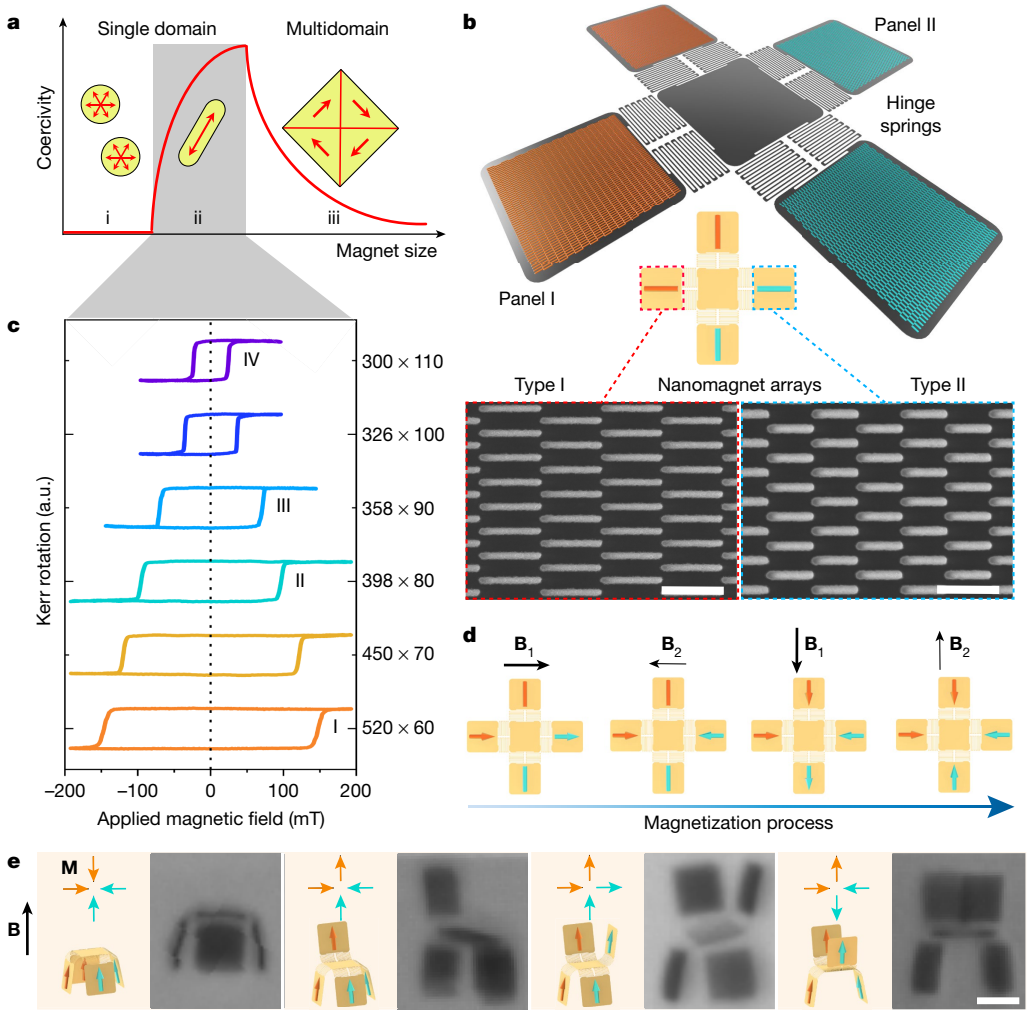


**Fig. 1 | Design of a four-panel shape-morphing micromachine. a**, Schematic diagram of the magnetic states found in magnets with increasing size: i, superparamagnetic; ii, stable single domain at room temperature; and iii, multidomain state. The red arrows indicate possible magnetization directions. The red trace schematically illustrates the size dependence of the coercivity of the magnets. Nanomagnets in region ii (the shaded area) are implemented in this work. **b**, Top, four-panel micromachine with an array of 520 nm × 60 nm (type I) nanomagnets on panel I and 398 nm × 80 nm (type II) nanomagnets on panel II; bottom, corresponding SEM images of the nanomagnet arrays. The zig-zag hinge spring has six turns. **c**, Magneto-optical Kerr effect hysteresis loops of single-domain nanomagnets with the same volume but with six different aspect ratios. The lateral dimensions are indicated to the right of the vertical axis in nanometres. The coercive fields of the type I–IV nanomagnets are $B_c(\mathrm{I}) \approx 140$ mT, $B_c(\mathrm{II}) \approx 90$ mT, $B_c(\mathrm{III}) \approx 70$ mT and $B_c(\mathrm{IV}) \approx 30$ mT. **d**, Schematic of the encoding of the micromachine using two fields, $B_1 > B_c(\mathrm{I})$ (large enough to switch type I and type II nanomagnets) and $B_c(\mathrm{I}) > B_2 > B_c(\mathrm{II})$ (large enough to switch type II, but not type I, nanomagnets) applied along both the horizontal and vertical directions (see main text for details). **e**, Schematics of the magnetic configurations (with type I and type II nanomagnets) and micromachine folding behaviour on application of the controlling magnetic field $B = 15$ mT, with optical microscope images showing the four different conformations of the fabricated devices. Going from left to right, the numbers of panels folding up/down are 4/0, 3/1, 2/2 (opposite panels having different folding directions) and 2/2 (opposite panels having the same folding direction). Scale bars: 500 nm (**b**), 10 μm (all images in **e**).

The micromachine can then be encoded by a series of magnetizing fields, shown schematically in Fig. 1d. By applying a magnetic field $B_1 > B_c(\mathrm{I})$ along the $x$ direction, both type I and type II nanomagnets are magnetized with full remanent magnetization. A second, lower, magnetic field $B_c(\mathrm{I}) > B_2 > B_c(\mathrm{II})$ is then applied in the opposite direction to remagnetize the type II magnets in the opposite direction, so that the magnetization of the arrays on the two panels point head-to-head along the $x$ direction (orange and turquoise horizontal arrows in Fig. 1d). Similarly, applying $B_1$ and $B_2$ fields sequentially along the $y$ direction gives head-to-head magnetization for the other two panels, so that the device has all four panels magnetized towards the centre. Furthermore, using magnetizing field protocols with different combinations of $B_1$ and $B_2$ fields, the same micromachine can be magnetized into different magnetic configurations and, since each panel can be magnetized in one of two opposite directions, there are a total of $2^4 = 16$ magnetic configurations for the same micromachine.

After programming the magnetic configurations, the micromachine is released from the substrate (see Methods section 'Sample fabrication') and actuated with an applied magnetic field $\mathbf{B}$ that provides a magnetic torque $\boldsymbol{\tau} = \mathbf{m} \times \mathbf{B}$ on the panels, where $\mathbf{m}$ is the total magnetic moment of the nanomagnet arrays on a given panel. All of the panels patterned with nanomagnets try to align with the applied magnetic field direction, which is counterbalanced by the mechanical torque from the deformed hinge springs. (For spring designs and mechanical calculations, see Methods section 'Hinge spring design and properties' and Extended Data Fig. 3) When actuated by the controlling field, the four types of magnetic configuration give four distinct conformations, as shown in Fig. 1e and Supplementary Video 1. The transformations of our micromachines require actuation fields (<15 mT) that are smaller

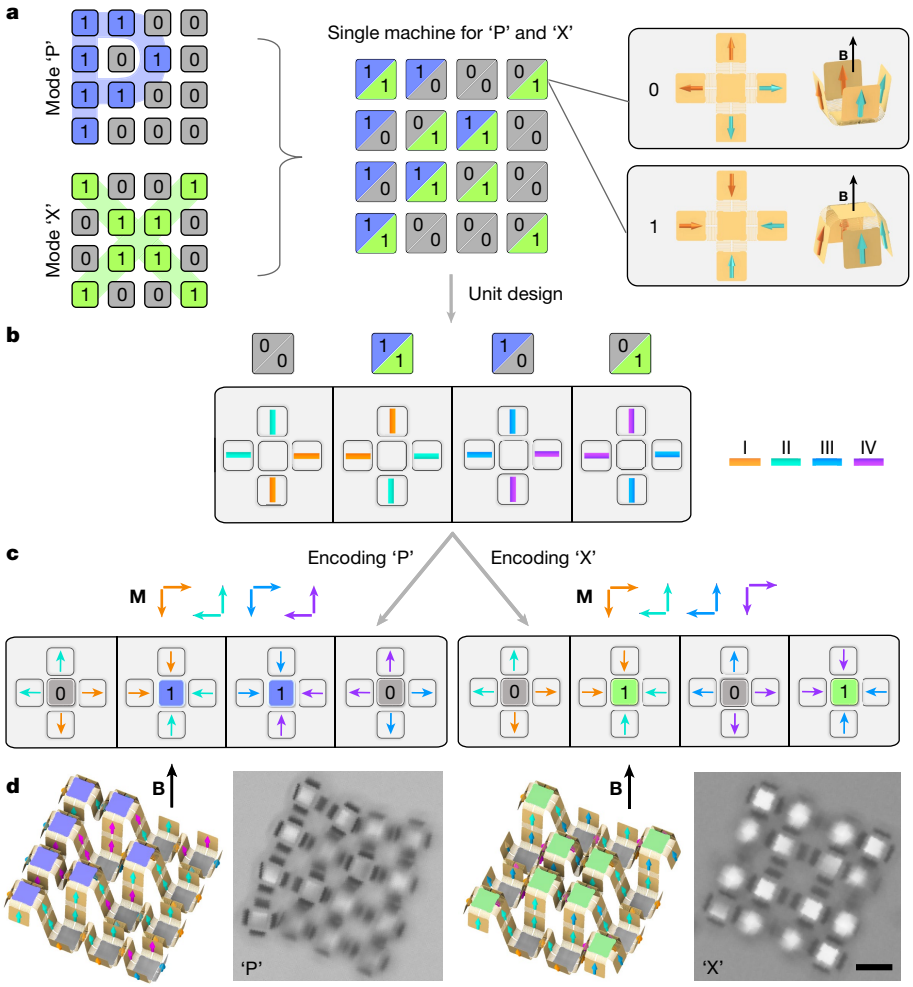


**Fig. 2 | Encoding letters of the alphabet into a shape-morphing micromachine assembled from an array of 4 × 4 four-panel units.** **a**, Conceptual design of a micromachine with 16 four-panel units that can be encoded to transform into letters 'P' and 'X', as illustrated by the pair of schematics on the left. Each box in the schematic represents a four-panel unit, where all the magnetizations of the panels in a given unit can be encoded to point outwards or inwards. Consequently, the central panel will move down or up when an out-of-plane controlling field $B$ is applied and we assign these to be the '0' state or the '1' state, respectively, as illustrated by the insets on the right. In order to combine mode 'P' and mode 'X' into a single micromachine, as illustrated by the central schematic, each unit is assigned one of four possible coding states given by (P, X) = (0, 0), (1, 1), (1, 0) or (0, 1). **b**, Design of the four different four-panel units with the four different coding states. Each panel contains an array of identical magnets whose orientation is given by the coloured bar on the panels. The colour of the bars corresponds to the colour of the hysteresis loops for the four different types of nanomagnets, I–IV, shown in Fig. 1c. **c**, Encoding the magnetization in the arrays of nanomagnets of the micromachine for the 'P' and 'X' shape morphing. The magnetization directions are given by the pairs of arrows labelled **M**, and the arrows within the boxes, which are coloured according to the four types of nanomagnet. **d**, Schematics and corresponding optical microscope images of the fabricated devices encoded for 'P' and 'X' shape morphing. The devices are actuated with $B$ = 15 mT. Scale bar (for both images), 20 µm.

than the switching fields, which are in the range 30–140 mT for the type I–IV nanomagnets. The complete set of shape transformations for all 16 magnetic configurations for this four-panel micromachine are shown in Extended Data Fig. 4. There are four distinct conformations (indicated by the four different background colours) due to the four-fold rotational symmetry of this particular micromachine. Nevertheless, the full programmability is given by the 16 different magnetic configurations, which can give additional conformations when assembling the micromachines into multicomponent devices or when using an asymmetric machine design. We have therefore demonstrated that, by encoding magnetic configurations through magnetizing field protocols, micromachines having the same structural design can be programmed with different shape-morphing behaviours.

Multicomponent shape-morphing micromachines can be constructed by assembling modular units such as the four-panel devices shown in Fig. 1e. We first built a micromachine by assembling the same modular units into a 3 × 3 array, which provides four distinct conformations (see Extended Data Fig. 5 and Supplementary Video 2). Furthermore, multiple tailored conformations can be attained by customizing the individual units and encoding their magnetic configurations. To demonstrate this, we engineered a micromachine that can transform to two distinct letters of the alphabet, 'P' and 'X', using different nanomagnetic encoding, as shown in Fig. 2. For this, we first selected a 4 × 4 assembly of the four-panel units (Fig. 2a) and, when applying the controlling magnetic field, each of the units moves either 'up' (magnetization on all four panels points inwards, represented by a '1' state), or 'down' (magnetization on all four panels points outwards, represented by a '0' state), with the set of '1'-state units representing a letter. Building both mode 'P' and mode 'X' into a single machine gives four distinct coding states—(P, X) = (0, 0), (1, 1), (1, 0) or (0, 1)—for each unit, where the first digit is associated with the 'P' mode and the second digit is associated with the 'X' mode. We created four types of assembly unit, each having one of the four coding states, which

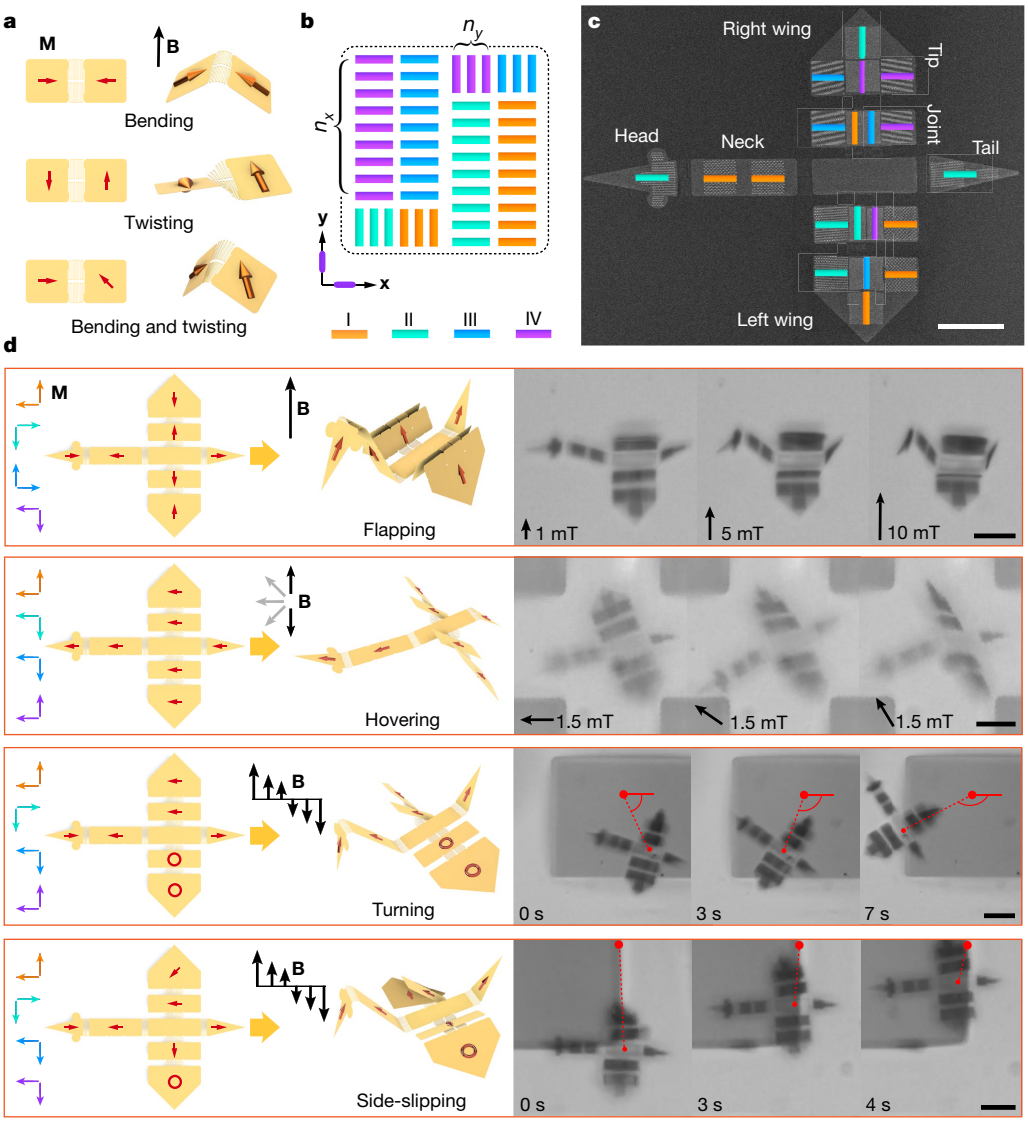


**Fig. 3 | Origami-like microscale 'bird' with multiple shape-morphing modes.** **a**, Schematic of the folding behaviours of two-panel devices when actuated using an applied out-of-plane magnetic field. These are achieved by setting the magnetization perpendicular, parallel or at an angle to the folding crease, as indicated by the red arrows on the panels. **b**, Schematic of the panel design using type I–IV nanomagnets with the magnet long axis oriented along *x* and *y* directions and the colour of the nanomagnets corresponding to the colours of the magnetic hysteresis loops in Fig. 1c. **c**, SEM image of the microscale 'bird'. The coloured bars indicate the location of the arrays of type I–IV nanomagnets and the orientation of the nanomagnets. **d**, Schematic (left) and optical images (right) of a microscale 'bird' mimicking four flying modes, 'flapping', 'hovering', 'turning' and 'side-slipping'. From left to right in each row: encoded magnetization direction (coloured arrows) of the type I–IV nanomagnets with the colours corresponding to the colours of the magnetic hysteresis loops in Fig. 1c; schematic of a flat microscale 'bird' with the total magnetization direction for each panel indicated with red arrows; schematic showing the folding of the microscale 'bird' under the indicated controlling field **B**; and the optical microscope images of the experimental demonstrations. For 'flapping', the three optical images show the shape transformation in different controlling fields **B**. For 'hovering', shape transformations in a magnetic field (1.5 mT, 1 Hz), which rotates back and forth, are shown with the three optical images corresponding to three successive field directions during the field rotation. For 'turning', three successive snapshots of the shape transformations in an alternating magnetic field (11.6 mT, 24.5 Hz) are shown, and for 'side-slipping', three successive snapshots of the shape transformation in an alternating magnetic field (6.2 mT, 19.5 Hz) are shown. The solid black arrows indicate the direction of the applied magnetic field. In the optical images of the 'turning' and 'side-slipping' modes, a dashed red line connects a fixed reference point on the substrate (large red dot) and the middle point between the two wings of the 'bird' (small red dot), highlighting the motion of the 'bird'. Scale bars: **c**, 15 μm; **d**, 30 μm.

was achieved using different combinations of arrays of the four types of nanomagnet, I–IV (Fig. 2b). The micromachine was then constructed from these four assembly units, corresponding to the arrangement of the coding states shown in Fig. 2a. The micromachine is then encoded so that one set of magnetic configurations of the units represents 'P' and the other represents 'X' (Fig. 2c). After releasing the encoded devices from the substrate, the micromachines display shape-morphing into 'P' and 'X' patterns when actuated by an applied controlling field (see Fig. 2d and Supplementary Video 3). In addition to these two patterns, this micromachine design also has '9' and '0' modes, which are conjugate modes of 'P' and 'X' modes, respectively (see Extended Data Fig. 6). This modular design concept can therefore be used to create complex shape-morphing systems with tailored three-dimensional (3D) transformations by customizing the design and layout of the functional units.

More advanced folding behaviours, such as the bending and twisting shown in Fig. 3a, can be achieved by programming the rigid panels of the shape-morphing micromachines with arbitrary magnetic configurations. The magnetic moment of the panels can be tuned by including arrays of nanomagnets with different aspect ratios and orientations (see Methods section 'Design of nanomagnet arrays'). In the example shown in Fig. 3b, with four types of nanomagnet I–IV oriented along both the $x$ and $y$ directions, there are $2^4 \times 2^4 = 2^8$ magnetic configurations on a single panel. By adjusting the quantities $n_x$ and $n_y$ of each type of nanomagnet along the $x$ and $y$ directions, it is possible to assign to each panel a total magnetic moment of almost arbitrary magnitude and direction. As a demonstration, we have engineered an origami-like microscale 'bird' to mimic the different flying modes of a real bird (see Fig. 3c). This is achieved with specific arrangements of the nanomagnet arrays on the five body parts—head, neck, body, tail and a pair of wings. For the tips and joints of the bird's wings, there are four arrays of nanomagnets on each panel with different orientations and switching fields. Therefore the total magnetization on these panels has eight possible directions and one demagnetized state (see Extended Data Fig. 7). By encoding the nanomagnets on the microscale 'bird' with different magnetic configurations, we demonstrate four distinct morphological transformations—'flapping', 'hovering', 'turning' and 'side-slipping' (see Fig. 3d and Supplementary Videos 4–7)—achieved by varying the magnetic fields, as indicated in Fig. 3d. Here advanced folding behaviours are demonstrated; for the 'hovering' mode, the left and right wings 'twist' relative to the body, and in the 'side-slipping' mode, the right wing tip 'bends and twists' relative to the right wing joint. Ways to achieve additional transformations are discussed in Methods section 'Further transformations'.

For future applications, our micromachines have a wide range of tunability in terms of size, ranging from submicrometre-sized panels with a single nanomagnet up to millimetre-sized devices: this range is limited only by the fabrication methods available. The nanomagnet arrays can be further engineered to have temperature-dependent magnetic properties[24], and they can be modulated using radio-frequency magnetic fields[25] and light[26]. This possibility of control with several different stimuli provides further functionality of the micromachines in many different environments. Nanoscale magnets switch in only a few nanoseconds[25], which is much faster than the mechanical response of the micromachines that occurs on the millisecond timescale[15]. Therefore, the micromachines can be reprogrammed in situ using a short (nanosecond to millisecond) magnetic field pulse. With the ability to precisely control transformations at the micrometre scale, our micromachines also offer a platform to construct 3D magnetic metamaterials[27], such as a 3D realization of artificial spin ice[28], and photonic metamaterials[29], where optical properties, such as the polarization of transmitted light, can be tuned by magnetically actuated transformations. This concept can also be applied in flexible electronics, with morphable 3D structures having multistable states[30]. By encoding the nanomagnets, the devices can be readily switched between these states using an applied magnetic field.

## Online content

Any methods, additional references, Nature Research reporting summaries, source data, extended data, supplementary information, acknowledgements, peer review information; details of author contributions and competing interests; and statements of data and code availability are available at https://doi.org/10.1038/s41586-019-1713-2.


1. Nelson, B. J., Kaliakatsos, I. K. & Abbott, J. J. Microrobots for minimally invasive medicine. *Annu. Rev. Biomed. Eng.* **12**, 55–85 (2010).
2. Li, J., Esteban Fernández De Ávila, B., Gao, W., Zhang, L. & Wang, J. Micro/nanorobots for biomedicine: delivery, surgery, sensing, and detoxification. *Sci. Robot.* **2**, eaam6431 (2017).
3. Rus, D. & Tolley, M. T. Design, fabrication and control of soft robots. *Nature* **521**, 467–475 (2015).
4. Rich, S. I., Wood, R. J. & Majidi, C. Untethered soft robotics. *Nat. Electron.* **1**, 102–112 (2018).
5. Palagi, S. & Fischer, P. Bioinspired microrobots. *Nat. Rev. Mater.* **3**, 113–124 (2018).
6. Hu, C., Pané, S. & Nelson, B. J. Soft micro- and nanorobotics. *Annu. Rev. Control. Robot. Auton. Syst.* **1**, 53–75 (2018).
7. Zheludev, N. I. & Kivshar, Y. S. From metamaterials to metadevices. *Nat. Mater.* **11**, 917–924 (2012).
8. Xia, F. & Jiang, L. Bio-inspired, smart, multiscale interfacial materials. *Adv. Mater.* **20**, 2842–2858 (2008).
9. Miskin, M. Z. et al. Graphene-based bimorphs for micron-sized, autonomous origami machines. *Proc. Natl Acad. Sci. USA* **115**, 466–470 (2018).
10. Kim, Y., Yuk, H., Zhao, R., Chester, S. A. & Zhao, X. Printing ferromagnetic domains for untethered fast-transforming soft materials. *Nature* **558**, 274–279 (2018).
11. Sydney Gladman, A., Matsumoto, E. A., Mahadevan, L., Nuzzo, R. G. & Lewis, J. A. Biomimetic 4D printing. *Nat. Mater.* **15**, 413–418 (2016).
12. Huang, H.-W., Sakar, M. S., Petruska, A. J., Pane, S. & Nelson, B. J. Soft micromachines with programmable motility and morphology. *Nat. Commun.* **7**, 12263 (2016).
13. Magdanz, V., Guix, M., Hebenstreit, F. & Schmidt, O. G. Dynamic polymeric microtubes for the remote-controlled capture, guidance, and release of sperm cells. *Adv. Mater.* **28**, 4084–4089 (2016).
14. Jin, D. et al. Four-dimensional direct laser writing of reconfigurable compound micromachines. *Mater. Today* https://doi.org/10.1016/j.mattod.2019.06.002 (2019).
15. Peyer, K. E., Zhang, L. & Nelson, B. J. Bio-inspired magnetic swimming microrobots for biomedical applications. *Nanoscale* **5**, 1259–1272 (2013).
16. Erb, R. M., Martin, J. J., Soheilian, R., Pan, C. & Barber, J. R. Actuating soft matter with magnetic torque. *Adv. Funct. Mater.* **26**, 3859–3880 (2016).
17. Hu, W., Lum, G. Z., Mastrangeli, M. & Sitti, M. Small-scale soft-bodied robot with multimodal locomotion. *Nature* **554**, 81–85 (2018).
18. Xu, T., Zhang, J., Salehizadeh, M., Onaizah, O. & Diller, E. Millimeter-scale flexible robots with programmable three-dimensional magnetization and motions. *Sci. Robot.* **4**, eaav4494 (2019).
19. Kim, J. et al. Programming magnetic anisotropy in polymeric microactuators. *Nat. Mater.* **10**, 747–752 (2011).
20. Huang, T. Y. et al. 3D Printed microtransporters: compound micromachines for spatiotemporally controlled delivery of therapeutic agents. *Adv. Mater.* **27**, 6644–6650 (2015).
21. Cowburn, R. P., Koltsov, D. K., Adeyeye, A. O. & Welland, M. E. Single-domain circular nanomagnets. *Phys. Rev. Lett.* **83**, 1042–1045 (1999).
22. Cowburn, R. P. Property variation with shape in magnetic nanoelements. *J. Phys. D* **33**, R1–R16 (2000).
23. Rus, D. & Tolley, M. T. Design, fabrication and control of origami robots. *Nat. Rev. Mater.* **3**, 101–112 (2018).
24. Gliga, S. et al. Emergent dynamic chirality in a thermally driven artificial spin ratchet. *Nat. Mater.* **16**, 1106–1111 (2017).
25. Barros, N., Rassam, M., Jirari, H. & Kachkachi, H. Optimal switching of a nanomagnet assisted by microwaves. *Phys. Rev. B* **83**, 144418 (2011).
26. Lambert, C. H. et al. All-optical control of ferromagnetic thin films and nanostructures. *Science* **345**, 1337–1340 (2014).
27. Fernández-Pacheco, A. et al. Three-dimensional nanomagnetism. *Nat. Commun.* **8**, 15756 (2017).
28. Heyderman, L. J. & Stamps, R. L. Artificial ferroic systems: novel functionality from structure, interactions and dynamics. *J. Phys. Condens. Matter* **25**, 363201 (2013).
29. Gansel, J. K. et al. Gold helix photonic metamaterial as broadband circular polarizer. *Science* **325**, 1513–1515 (2009).
30. Fu, H. et al. Morphable 3D mesostructures and microelectronic devices by multistable buckling mechanics. *Nat. Mater.* **17**, 268–276 (2018).

# Methods

### Sample fabrication

A schematic of the fabrication process can be found in Extended Data Fig. 8. The samples were fabricated on a 50-nm-thick low-stress silicon nitride membrane (Silson Ltd, UK) supported by a rigid silicon frame. First, the nanomagnets were fabricated on the membrane with electron beam lithography using an electron beam writer (Vistec EBPG 5000PlusES) to pattern a spin-coated 50k poly(methylmethacrylate) (PMMA)/950k PMMA double-layer. A magnetic film of 5 nm Ti (adhesion layer)/60 nm Co/3 nm Al (capping layer) was thermally evaporated at a base pressure of ~$1 \times 10^{-6}$ mbar onto the patterned resist, which was followed by a lift-off process in acetone. Then the panels were fabricated by spin-coating a 950k PMMA layer on the front of the silicon nitride membrane, which was then patterned using electron beam lithography in order to define the geometry of the rigid panels and hinge springs of the micromachines. After coating a second 950k PMMA layer on the back of the membrane, reactive ion etching (RIE, Oxford PlasmaPro 100) was performed on the front side to etch through the 50-nm-thick silicon nitride membrane. After the RIE process, the fabricated micromachines were only supported by the free-standing PMMA layer coated on the back of the membrane. The devices were then magnetized by a sequence of magnetic fields and released in an organic solvent, propylene glycol monomethyl ether acetate (PGMEA). A further discussion of this release process and possible operation of the micromachines in other media can be found in Methods section 'Micromachine release and operation'. The SEM (Zeiss Supra VP55) images were taken with a 3–10 kV acceleration voltage.

### Magnetic characterization and encoding

The nanomagnets were characterized with MOKE measurements using a commercial setup (NanoMOKE, Durham Magneto Optics Ltd.) in the longitudinal mode with a focused laser spot with a diameter of ~10 μm. Each hysteresis loop was obtained by averaging ten measurements. The nanomagnet arrays were encoded using the magnetizing field from the electromagnet in the NanoMOKE setup. The electromagnet was equipped with a manual rotation stage to hold the sample between the electromagnet iron poles. By rotating the sample on this stage, a magnetic field of up to 400 mT could be applied in any direction in the sample plane.

### Magnetic manipulation

After the sample fabrication and the magnetic field encoding, the sample was released in an organic solvent (PGMEA) while being observed with an optical microscope incorporating three pairs of Helmholtz coils in an orthogonal configuration. A computer was used to simultaneously control the electric currents in the three-pair Helmholtz coils to produce a magnetic field vector in arbitrary 3D directions. A magnetic field with a maximum magnitude of 15 mT was generated to manipulate the released micromachines. The observed folding behaviour and motion were captured with a video camera (Grasshopper GRAS-03K2C, Point Grey Research) on the microscope. The tested micromachines were actuated reversibly with a dynamic field more than 18,000 times (30 Hz, 10 min) with no observable signs of plastic deformation or breaking.

### Nanomagnet design and coercivity

The magnetic domain state of an element made of a soft polycrystalline ferromagnetic material (typically Fe, Ni and Co) is dictated by the competition between the quantum mechanical exchange energy and the stray field energy that is size- and shape-dependent[31]. By varying the lateral size and shape, it is possible to create single-domain nanomagnets.

The nanomagnets are designed in a stadium shape, comprising a rectangle with one semi-circle at each end, with the width of the rectangle matching the semi-circle diameter, as shown in Extended Data Fig. 2a. This shape ensures that the remanent magnetization is parallel to the long axis of the magnets, pointing in one of the two directions. The volume of the stadium-shaped nanomagnet is given by:

$$V = \left[ d(L-d) + \pi\left(\frac{d}{2}\right)^2 \right] t \tag{1}$$

When the length, width and thickness of the nanomagnets are $L = 300$ nm, $d = 110$ nm and $t = 60$ nm, respectively, the volume of the nanomagnet is $V_0 = 1.82 \times 10^{-21}$ m$^3$. The total magnetic moment of a nanomagnet is given by $m = MV$, where $M$ is the saturation magnetization of the magnetic material. In this work, 60-nm-thick cobalt nanomagnets are employed, and the saturation magnetization of the thermally evaporated Co thin film is $M_s = 1{,}153$ kA m$^{-1}$, measured using a superconducting quantum interference device vibrating sample magnetometer (SQUID VSM) at room temperature.

Nanomagnets with different aspect ratios, $L/d$, display different magnetic coercivities, as shown in Fig. 1c. Here we keep the same nanomagnet volume $V_0$ and thickness $t_0 = 60$ nm for all nanomagnets regardless of the aspect ratio. Therefore, they have the same magnetic moment $m_0 = MV_0$ and equation (1) can be modified to read:

$$V_0 = \left[ d(L-d) + \pi\left(\frac{d}{2}\right)^2 \right] t_0 \tag{2}$$

So that the relation between $L$ and $d$ is given by:

$$L = d + \frac{\frac{V_0}{t_0} - \pi\left(\frac{d}{2}\right)^2}{d} \tag{3}$$

A plot of $d$ against $L$, determined using equation (3), is shown in Extended Data Fig. 2c. In this figure, nanomagnets with the same volume $V_0$ but with six different aspect ratios are selected, that is, with lateral dimensions of 520 nm × 60 nm, 450 nm × 70 nm, 398 nm × 80 nm, 358 nm × 90 nm, 326 nm × 100 nm and 300 nm × 110 nm. The layout of the nanomagnet arrays is schematically shown in Extended Data Fig. 2b, with a spacing of $d/2$ in the $x$ direction. In this layout, the dipolar coupling between the nanomagnets supports parallel alignment of the magnetization between neighbouring magnets. In the $y$ direction, neighbouring nanomagnets are separated by a distance $s = 40$ nm for all nanomagnet arrays.

SEM images of the fabricated arrays are given in Extended Data Fig. 2e. The MOKE magnetic characterization is shown in Fig. 1c, with the square shapes of the hysteresis loops confirming the single-domain magnetic state of the nanomagnets. Since all nanomagnets investigated in this study have same magnetic moment, $m_0 = 2.10 \times 10^{-15}$ A m$^2$, the total magnetic moment of the nanomagnet arrays on an individual panel (when all magnetizations are aligned in the same direction) is

$$m_{\text{total}} = n_{\text{magnets}} m_0 \tag{4}$$

where $n_{\text{magnets}}$ is the number of nanomagnets on the panel. For the device demonstrated in Fig. 1, a total of 1,040 nanomagnets are fabricated on each panel, with $m_{\text{total}} = 2.18 \times 10^{-12}$ A m$^2$ pointing parallel to the long axis of the nanomagnets.

The square shapes of the hysteresis loops measured using the MOKE, shown in Fig. 1c, indicate that all six types of designed nanomagnets are fully magnetized at remanence. As shown by the MOKE curves in Extended Data Fig. 2d, the magnetic switching occurs over a relatively small field range of 5–20 mT. Since the six transition regions do not overlap, all six types of nanomagnets can be individually programmed, even for a micromachine containing arrays of all six nanomagnets oriented in the same direction.

### Hinge spring design and properties

Inspired by the art of origami, we have designed rigid panels carrying single-domain nanomagnets, connected by structured hinge springs acting as folding creases. The hinge spring layout needs to be designed so that there is a considerable folding behaviour on the application of a small magnetic field, $B < 15$ mT.

We first derive the relationship between applied magnetic field $B$ and panel rotation angle $\theta$. Neglecting the bending of the short sections of the spring, the twisting of the zig-zag spring can be determined by considering a long and slender beam of equivalent length that can twist subject to an applied torque.

Considering first the twist of an isolated beam with uniform cross-section along its length (see Extended Data Fig. 3a), the angle of twist in radians is given by $\theta = \frac{\tau L}{GJ}$, where $\tau$ is the applied torque, $L$ is the beam length, and $G$ and $J$ are the shear modulus and torsional constant of the material, respectively.

For a beam with a rectangular section, the torsional constant is given by

$$J = \frac{wt(w^2 + t^2)}{12} \tag{5}$$

where $w$ and $t$ are the side lengths[32]. For a homogeneous isotropic material,

$$G = \frac{E}{2(1+\nu)} \tag{6}$$

where $E$ is the Young's modulus and $\nu$ is the Poisson ratio. Hence the panel rotation angle is given by:

$$\theta = \frac{24(1+\nu)L}{Ewt(w^2 + t^2)}\tau \tag{7}$$

The applied torque is given by $\tau = k\theta$, so that the magnitude of the torsional spring constant, $k$, is given by

$$k = \frac{Ewt(w^2 + t^2)}{24(1+\nu)L} \tag{8}$$

For the current design, the total length of such a beam is $L = nl$, where $l$ is the length of each beam section and $n$ is the total number of beam sections. Therefore, for each spring:

$$k_s = \frac{Ewt(w^2 + t^2)}{24(1+\nu)nl} \tag{9}$$

If two springs are used and they are in a parallel configuration:

$$k_{total} = k_s + k_s = \frac{Ewt(w^2 + t^2)}{12(1+\nu)nl} \tag{10}$$

Taking into account that the direction of panel rotation $\theta$ is opposite to the direction of the mechanical torque induced on the spring, the total torque on the spring is given by:

$$\tau_{spring} = -k_{total}\theta \tag{11}$$

We now determine the extent of the folding in a magnetic field for hinge designs with different numbers of turns in our micromachines. For this, we have fabricated simple two-panel devices to investigate the relationship between the applied magnetic field and the panel rotation angle. An SEM image of an eight-turn two-panel device is shown in Extended Data Fig. 3b. The fabricated devices have identical arrays of nanomagnets (398 nm × 80 nm nanomagnets on the left panel and 520 nm × 60 nm nanomagnets on the right panel) but the number of turns in the hinge spring is varied, with $q = 2, 4, 6$ and 8; see Extended Data Fig. 3c. The total length of each spring is therefore $L = nl = (2q+1)l$, where $l = 5$ µm is the length of each section of the spring.

According to the illustration in Extended Data Fig. 3d, the magnetic-field-induced torque on the device is $\boldsymbol{\tau}_B = \mathbf{m} \times \mathbf{B}$ and its magnitude is:

$$\tau_B = mB\sin(90^\circ - \theta) = mB\cos\theta \tag{12}$$

At equilibrium:

$$\tau_B + \tau_{spring} = 0 \tag{13}$$

Introducing equations (11) and (12) into equation (13) gives:

$$mB\cos(\theta) - k_{total}\theta = 0$$

$$\frac{\theta}{\cos\theta} = \frac{m}{k_{total}}B \tag{14}$$

Introducing equations (4) and (10) into equation (14), we obtain:

$$\frac{\theta}{\cos\theta} = \frac{n_{magnets}m_0 12(1+\upsilon)nl}{Ewt(w^2 + t^2)}B \tag{15}$$

This equation is the relation between applied magnetic field $H$ and panel rotation angle $\theta$, which can be numerically solved. Here $n_{magnets} = 1{,}175$, $n = [5, 9, 13, 17]$ for devices with 2-, 4-, 6- and 8-turn hinges, and the lateral dimensions are $w = 100$ nm, $t = 50$ nm and $l = 5$ µm, as used in the experimental micromachines. From equation (4), the total magnetic moment on each panel is $m_{total} = 2.47 \times 10^{-12}$ A m$^2$. Shown in Extended Data Fig. 3e are optical microscope images of the panel rotation for hinged spring designs with different numbers of turns following actuation in the same field, $B = 5$ mT. The experimental demonstrations and computational results are plotted in Extended Data Fig. 3f, g, respectively, and follow similar trends. The panel rotation angle is larger in the experiment, which may be partly due to over-etching in the final nanofabrication step leading to hinged springs that are narrower than in the original design. For the devices shown in Figs. 1–3, hinge springs with $q = 6$ turns were used. With the current possibilities for magnetic field control of field steps of 0.1 mT, we can orient the panels to within ~0.1° to 1°, depending on the panel rotation angle in an applied magnetic field.

We now estimate the magnitude of the largest torque and force that can be generated from the panels patterned with nanomagnets. The induced mechanical torque on the panels $\tau$ has a linear relationship with the magnitude of the applied magnetic field $B$, since $\boldsymbol{\tau} = \mathbf{m} \times \mathbf{B}$. However, on increasing $B$, the mechanical torque $\tau$ cannot be infinitely high, since the applied magnetic field may switch the nanomagnets. For example, if the magnetic field is applied along the long axis of the magnets, then it can alter the magnetization if it is larger than the switching field, which is 30 mT for the type IV nanomagnets.

For a given micromachine, there are several panels in different orientations that change as the magnetic field is applied. We therefore assume that we can safely operate a machine with an upper limit to the field given by the coercive field $B_c$, that is, the switching field of the magnets when applying a field parallel to the magnet long axis.

We calculate the torque and force that can be generated by a panel patterned with type IV nanomagnets. For the four-panel devices and their modular assemblies in Figs. 1, 2, there are in total 1,040 nanomagnets on each 10 µm × 10 µm panel, with $m_{total} = 2.18 \times 10^{-12}$ A m$^2$ pointing along the long axis of the nanomagnets. In this case, for a 30 mT operation field, the highest generated magnetic torque is $\tau = (2.18 \times 10^{-12}\,\text{A m}^2) \times (30\,\text{mT}) \times \sin(90°) = 6.54 \times 10^{-14}$ N m. Assuming one edge of the panel

is hinged, then the highest generated force is $f = (6.54 \times 10^{-14}\ \text{N m})/(10\ \mu\text{m}) = 6.54 \times 10^{-9}\ \text{N} = 6.54\ \text{nN}$.

Similarly, for a 10 μm × 10 μm panel patterned with type I nanomagnets, which have a switching field of 140 mT, the highest generated mechanical torque is $\tau = 3.05 \times 10^{-13}$ N m, and the highest generated force is $f = 30.5$ nN.

It has been shown previously that microrobots can be used to move cells by pushing them with forces in the piconewton range[33]. For moving even larger objects, such as a 100 μm × 10 μm × 8 μm microbar, it has been shown that ~200 pN of force is needed[34]. Therefore, since our machines can supply forces up to several nanonewtons, they are capable of manipulating biological objects such as cells.

### Design of nanomagnet arrays

We engineer the orientation and magnitude of the magnetic moment of the arrays of nanomagnets. Here, we can consider a panel consisting of nanomagnets with $p$ different aspect ratios, each with different switching fields $B_{c,i}$ and magnetic moments $m_i = M_i V_i$, where $i = 1, 2, \ldots, p$. $M_i$ is the magnetization of the magnetic material and $V_i$ is the volume of the nanomagnet. The nanomagnets with magnetic moment $m_i$ can be fabricated with several different arbitrary orientations $\phi_{i,j}$ on a panel. Here, $j = 1, 2, \ldots, k_i$, where $k_i$ denotes the total number of different orientations for the nanomagnets with magnetic moment $m_i$. Therefore, we obtain the total magnetic moment $m_{\text{total}}$ for all arrays of nanomagnets on a given panel

$$m_{\text{total}} = \sum_{i=1}^{p} \sum_{j=1}^{k_i} n_{i,j} m_i (\cos\varphi_{i,j} + i\sin\varphi_{i,j}) \tag{16}$$

where $n_{i,j}$ is the quantity of the nanomagnets with magnetic moment $m_i$ and orientation $\phi_{i,j}$. This total magnetic moment, $m_{\text{total}}$, of nanomagnets on a single panel can be programmed with arbitrary magnitude and direction by careful adjustment of the magnetic moment $m_i = M_i V_i$, orientations $\phi_{i,j}$ and quantities $n_{i,j}$ of the nanomagnets.

In our micromachines, both the magnetization $M_i$ and the volume $V_i$ of the nanomagnets are the same for nanomagnets with different switching fields, so we can assume that magnitude of the magnetic moment $m_i = M_i V_i$ of all magnets in the array are the same, that is, $m_i = M_i V_i = M_0 V_0 = m_0$. Therefore, equation (16) can be simplified to:

$$m_{\text{total}} = m_0 \sum_{i=1}^{p} \sum_{j=1}^{k_i} n_{i,j} (\cos\varphi_{i,j} + i\sin\varphi_{i,j}) \tag{17}$$

In our systems, the nanomagnets only have two orientations, which are orthogonal to each other. This means that the magnets in the two orthogonal arrays can be magnetized independently by applying a field parallel to the long axes of the nanomagnets in one of the arrays. To be specific, in our design, the long axis of each magnet is aligned along one of two orientations, that is, parallel to one of the two coordinate axes ($x$ or $y$ axis, so $k_i = 2$). Therefore, the magnetization of the nanomagnets can point along one of four cardinal directions (North, South, East and West) so that the orientation of the total magnetic moment is given by

$$\varphi = \tan^{-1} \frac{\sin\varphi_{i,y} \sum_{i=1}^{p} n_{i,y}}{\cos\varphi_{i,x} \sum_{i=1}^{p} n_{i,x}} \tag{18}$$

where $n_{i,x}$, $n_{i,y}$ are the number of $i$ types of nanomagnets with a given switching field with the long axis along the $x$ and $y$ axis, respectively, so that $\varphi_{i,x} = 0, \pi$ and $\varphi_{i,y} = \pm\frac{\pi}{2}$ depending on the direction of magnetization in the nanomagnets. According to equation (18), by changing the number of magnets with a given orientation, that is, $n_{i,x}$ and $n_{i,y}$, it is possible to obtain an arbitrary orientation $\phi$ of the total magnetic moment $m_{\text{total}}$.

For each panel, there are nanomagnets with $p_x$ and $p_y$ different switching fields along the $x$ and $y$ axis, respectively. It is therefore possible to program $2^{p_x} \times 2^{p_y}$ magnetic configurations, which have a total magnetic moment with a particular magnitude and orientation. In order to encode a panel with two or more different types of nanomagnet, one starts by magnetizing the highest-coercivity magnet, so that all magnets on the panel will be magnetized in the direction of the field. If required, the lower-coercivity magnets can be oppositely magnetized using a magnetic field applied in the reverse direction that is sufficiently low to leave the higher-coercivity nanomagnets unaffected.

### Further transformations

In this article, the transformations are inspired by origami, and the micromachines are constructed with rigid panels and structured soft creases. The rigid panels carry the programmed nanomagnet arrays, which provide the mechanical torque for transformations when an external magnetic field is applied. Here, the nanomagnets are designed to be stadium-shaped, with the remanent magnetization pointing in the plane of the rigid panel along the geometric long axis of the magnets as a result of the magnetic shape anisotropy.

The current concept has limitations where folding into particular shapes is not straightforward. For example, the four-panel devices shown in Fig. 1, which have all four side panels magnetized towards or away from the centre, can achieve folding into an 'uncovered box'. Shutting the lid to give a 'closed' box with an additional panel is not possible with the arrangement of nanomagnets used in this work. Instead, the magnetization of the nanomagnets on the lid needs to point out of the plane of the lid. This requires nanomagnets with out-of-plane magnetic anisotropy, which can be achieved with, for example, a Co/Pt multilayer system[35].

### Micromachine release and operation

We used organic solvents, such as PGMEA and acetone, to dissolve the PMMA supporting layer and release the micromachines from the silicon substrate in the final step of the fabrication process. We chose PGMEA because it does not evaporate as fast as acetone and, in order to keep the experimental processes simple, we directly actuated the micromachines in the PGMEA solvent after the release. Nevertheless, the micromachines can also be operated in other working environments such as water and air and, since the nanomagnets have a 3 nm Al capping layer, they will not be easily oxidized. This 3 nm Al layer also ensures the biocompatibility of the micromachines. Here, we suggest three approaches to transfer and operate the structures in a water environment:

**Approach 1.** Instead of using a PMMA support layer coated on the back of the membrane (steps 3–4 in Extended Data Fig. 8), water-soluble coatings, such as poly(acrylic acid) or Dextran[36], can be used. These are compatible with microfabrication techniques and, after the RIE etching, the structures can be directly released and operated in water.

**Approach 2.** After the fabrication and the release of the structures in an organic solvent, the structures can be fished out and transferred to a water environment using a micromanipulator tip. This is a standard procedure for micro- and nano-robotic manipulation, and has been widely reported[20].

**Approach 3.** After the fabrication and the release of the structures in an organic solvent, water substitution can be performed, for example, in a Petri dish containing the solvent and the micromachines. This technique is widely used in soft or shape-morphing microrobotics[14]. It should be noted that PGMEA has limited miscibility with water. Therefore, if PGMEA is used to dissolve the PMMA for device release, acetone or isopropyl alcohol (IPA; fully miscible with PGMEA) can be used to substitute PGMEA first, and then a water substitution can be performed to replace acetone or IPA. An alternative approach is to directly use acetone to dissolve PMMA for device release, followed by a water substitution.

Using approach 3 with acetone to dissolve the PMMA, we have demonstrated operation of the four-panel device in water (see Extended Data Fig. 9a, b). In addition, we have demonstrated the manipulation of 6-μm-diameter polystyrene microbeads (Polybead 15714-5, Polysciences, Inc.) in a water environment (Extended Data Fig. 9c, d and Supplementary Video 8).

We have also demonstrated the operation of the micromachines in air. For this, we have fabricated single panels with one end attached by a hinge spring connection to a fixed silicon nitride membrane frame. In this case, both the PMMA support layer and the device release in PGMEA are not required, and the device is free to be manipulated in a magnetic field immediately after the reactive ion etching process. As shown in Extended Data Fig. 10 and Supplementary Video 9, on increasing an applied out-of-plane magnetic field, the panels fold upwards or downwards depending on the programmed magnetization direction of the nanomagnet arrays on each panel.

It is worth noting that, even without suspension in a solvent, the micromachines will not collapse due to the gravitational force. For the four-panel micromachine shown in Fig. 1, the weight is the combined weight of the silicon nitride membrane and the nanomagnets. The weight of silicon nitride panels is approximately given by $\rho_{SiNx} \times V_{SiNx} \times g = 7.8 \times 10^{-13}$ N, where $\rho_{SiNx} = 3.17$ g cm$^{-3}$ is the density of silicon nitride, $V_{SiNx} = 5 \times 10$ μm $\times 10$ μm $\times 50$ nm is the volume of the four-panel micromachine consisting of 5 rigid panels, and $g \approx 9.8$ m s$^{-2}$ is the standard gravity. The weight of the nanomagnets is approximately $\rho_{magnets} \times V_{magnets} \times g = 6.6 \times 10^{-13}$ N, where $\rho_{magnets} = 8.9$ g cm$^{-3}$ is the cobalt density, $V_{magnets} = 4 \times 1{,}040 \times V_0$ is the total volume of the nanomagnets on the micromachine with four side panels, each having 1,040 nanomagnets, and $V_0 = 1.82 \times 10^{-21}$ m$^3$ is the volume of each individual nanomagnet. Therefore the total weight of the four-panel micromachine is $7.8 \times 10^{-13}$ N + $6.6 \times 10^{-13}$ N = 1.44 pN. The magnitudes of the magnetic actuation force and the elastic force from the hinge springs are in the nanonewton range (as calculated in the Methods section 'Hinge spring design and properties'), which is three orders of magnitude larger than the gravitational load. Therefore the devices can be manipulated in air without structural collapse due to gravity.

## Data availability

All data generated or analysed during this study are included in the published article and its Supplementary Information, and are available from the corresponding authors on reasonable request.


31. O'Handley, R. C. *Modern Magnetic Materials: Principles and Applications* (Wiley, 1999).
32. Timošenko, S. P. & Goodier, J. N. *Theory of Elasticity* (McGraw-Hill, 1961).
33. Steager, E. B. et al. Automated biomanipulation of single cells using magnetic microrobots. *Int. J. Robot. Res.* **32**, 346–359 (2013).
34. Huang, T. Y. et al. Cooperative manipulation and transport of microobjects using multiple helical microcarriers. *RSC Advances* **4**, 26771–26776 (2014).
35. Luo, Z. et al. Chirally coupled nanomagnets. *Science* **363**, 1435–1439 (2019).
36. Linder, V., Gates, B. D., Ryan, D., Parviz, B. A. & Whitesides, G. M. Water-soluble sacrificial layers for surface micromachining. *Small* **1**, 730–736 (2005).



**Acknowledgements** J.C. received support from the European Union's Horizon 2020 Research and Innovation Programme under the Marie Skłodowska Curie Grant Agreement (number 701647). This work was financially supported by the European Research Council Advanced Grant–Soft MicroRobots (SOMBOT, number 743217), the Swiss National Science Foundation (number 200021_165564) and the National Natural Science Foundation of China (number 11702003). We thank A. Weber and V. Guzenko for helping with the development of the fabrication process. The sample fabrication was performed using the cleanroom facilities at the Laboratory for Micro- and Nanotechnology at the Paul Scherrer Institute, Switzerland.


**Author contributions** J.C., T.-Y.H., L.J.H. and B.J.N. conceived the project. J.C., Z.L., P.T. and X.-Z.C. developed the fabrication process. T.-Y.H., J.C., Z.L. and H.G. developed the design strategy of nanomagnetic encoding. T.-Y.H., J.C. and X.-Z.C. tested the shape-morphing performance. J.C., T.-Y.H. and L.J.H. worked on the manuscript together. All authors contributed to the discussion of the results and the manuscript revision.

**Competing interests** The authors declare no competing interests.


**Additional information**
**Supplementary information** is available for this paper at https://doi.org/10.1038/s41586-019-1713-2.
**Correspondence and requests for materials** should be addressed to J.C. or T.-Y.H.
**Peer review information** *Nature* thanks Je-Sung Koh, Xuanhe Zhao, and the other, anonymous, reviewer(s) for their contribution to the peer review of this work.
**Reprints and permissions information** is available at http://www.nature.com/reprints.

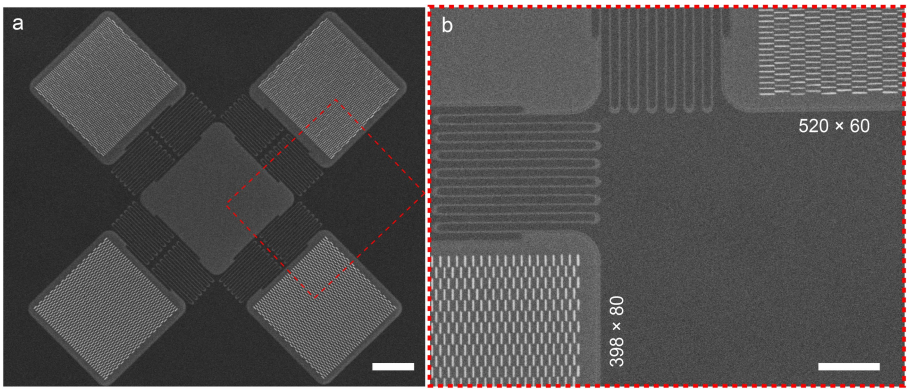


**Extended Data Fig. 1 | SEM images of a four-panel micromachine.** **a**, Overview. **b**, Enlarged image corresponding to the dashed box in **a**. Shown are arrays of nanomagnets: in the array at top right, the lateral dimension of each nanomagnet is 520 nm × 60 nm; at bottom left, the lateral dimension of each nanomagnet is 398 nm × 80 nm. Scale bars: **a**, 4 μm; **b**, 2 μm.

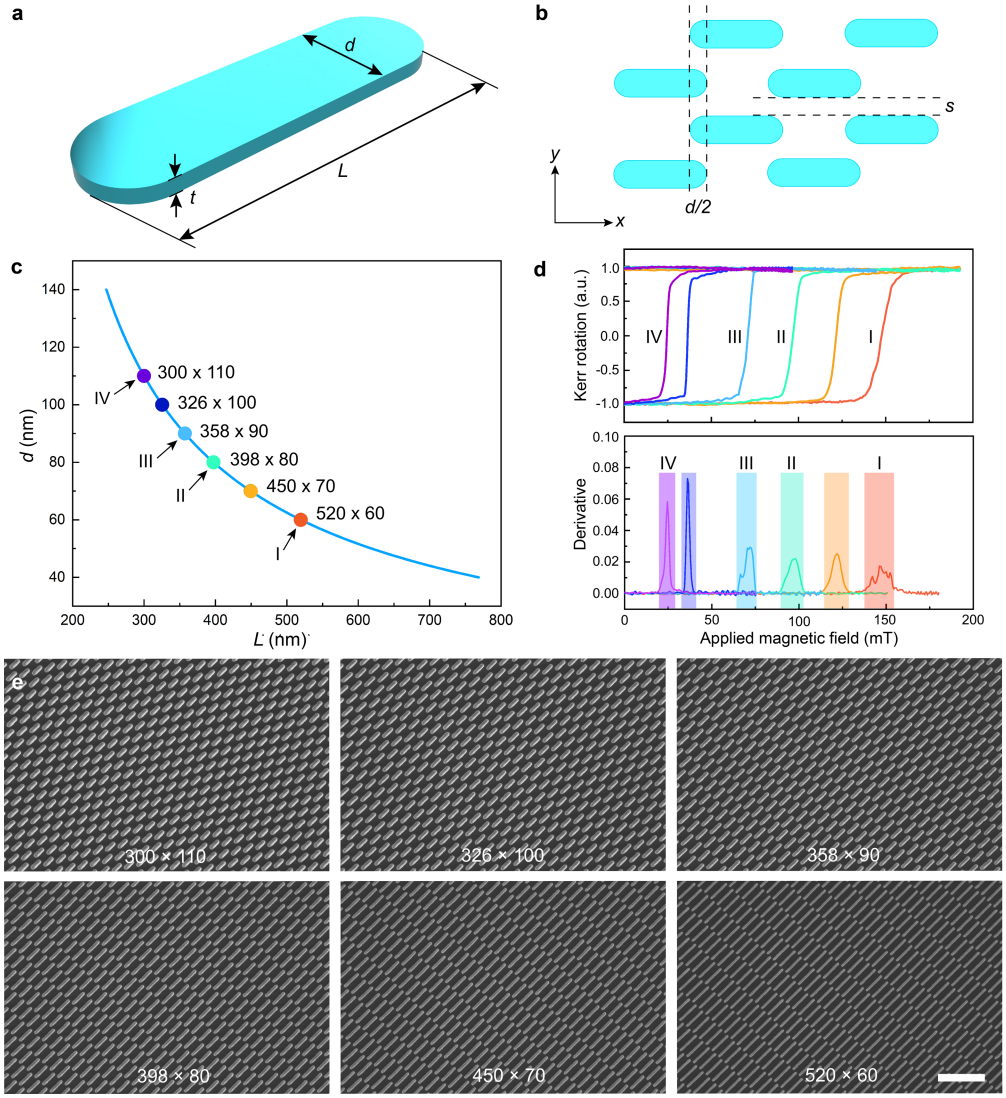


**Extended Data Fig. 2 | Geometric design and switching behaviour of the nanomagnets. a**, Schematic of a stadium-shaped nanomagnet with length $L$, width $d$ and thickness $t$. **b**, Schematic of the layout of the nanomagnet arrays with vertical separation $s$, and horizontal separation $d/2$. **c**, Relationship between $d$ and $L$ for nanomagnets with the same volume $V_0$ and thickness $t = 60$ nm. Six nanomagnets with different aspect ratios are indicated on the curve (the dimensions of each magnet are indicated in nm); the colour of the points corresponds to colour of the hysteresis loops in Fig. 1c. Arrows indicate the four types of nanomagnet used in the micromachines (I–IV). **d**, Magneto-optical Kerr effect curves for the six differently sized nanomagnets in the field region where they switch (top panel) and the derivative with the switching region highlighted with shaded boxes (bottom panel). As the six switching regions do not overlap, all six nanomagnets can be individually programmed. **e**, SEM images of fabricated arrays of nanomagnets with lateral dimensions given in nanometres, corresponding to the six coloured points in **c**. Scale bar at bottom right (1 µm) applies to all six images.

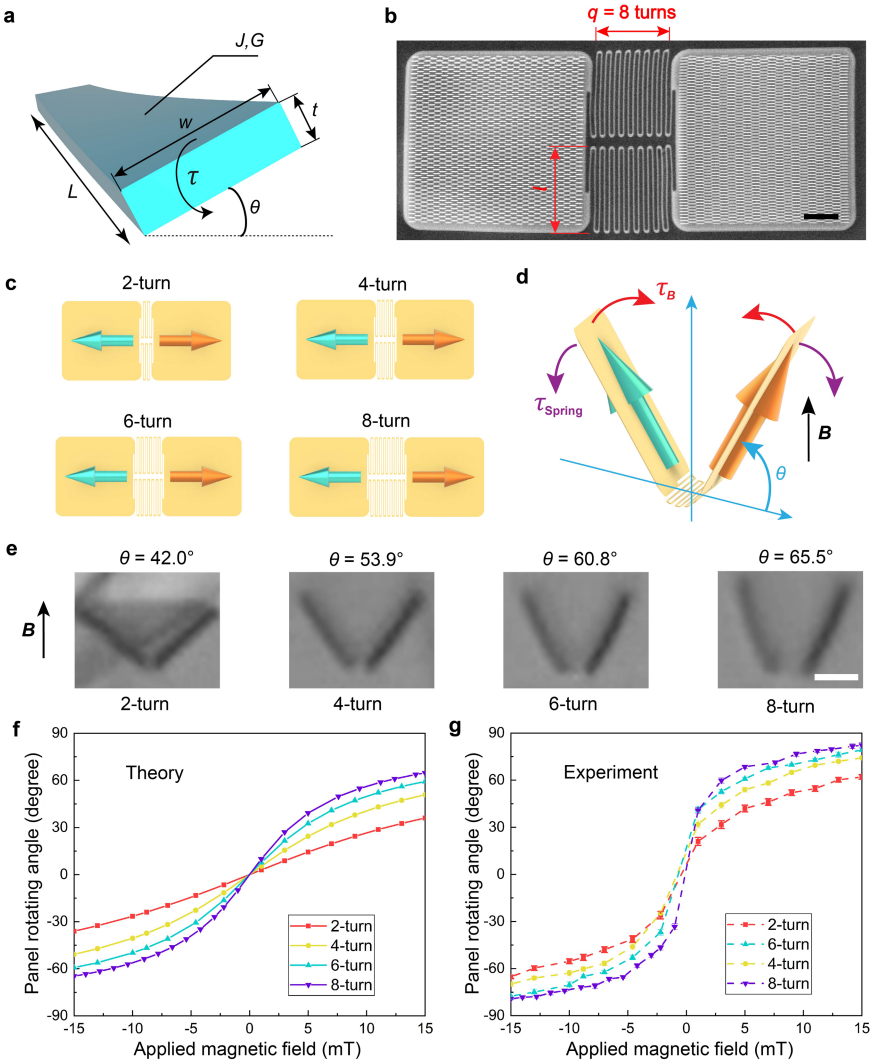


**Extended Data Fig. 3 | Hinge spring design. a**, Schematic of a single section of a spring. See Methods for nomenclature. **b**, SEM image of a two-panel device with an 8-turn spring. **c**, Schematic of two-panel devices with 2-, 4-, 6- and 8-turn spring designs. The turquoise and orange arrows represent the magnetization direction of the panels. **d**, Schematic of a two-panel device that folds when applying a controlling magnetic field ***B***. See Methods for nomenclature. **e**, Optical microscope images of four fabricated devices with different numbers of turns in the spring design on application of a 5 mT controlling field. **f**, Predicted panel rotating angle versus applied magnetic field based on theoretical calculations of the two-panel devices with different numbers of turns. **g**, Measured panel rotating angle versus applied magnetic field for the fabricated devices with different numbers of hinge spring turns. Each data point corresponds to the average of three measurements of the angle using image analysis software. Error bars, ±1 s.d. Scale bars: **b**, 2 µm; **e** (applies to all images in **e**), 5 µm.

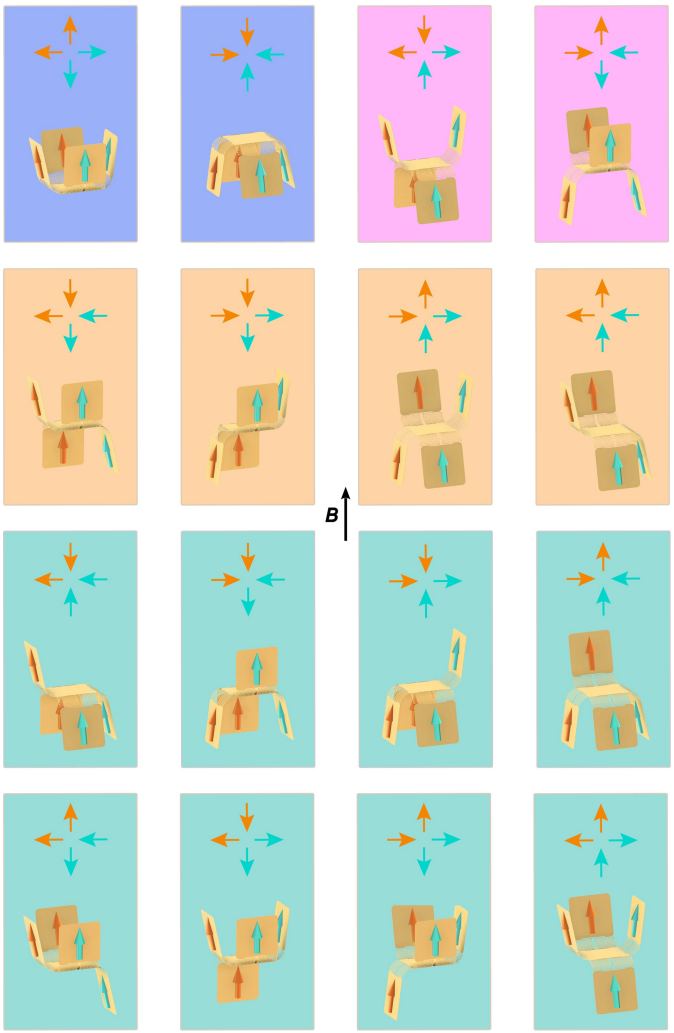


**Extended Data Fig. 4 | The 16 magnetization configurations of a four-panel micromachine and their corresponding shape transformation after applying a vertical controlling field.** The four background colours highlight the family of four distinct conformations demonstrated in Fig. 1c.

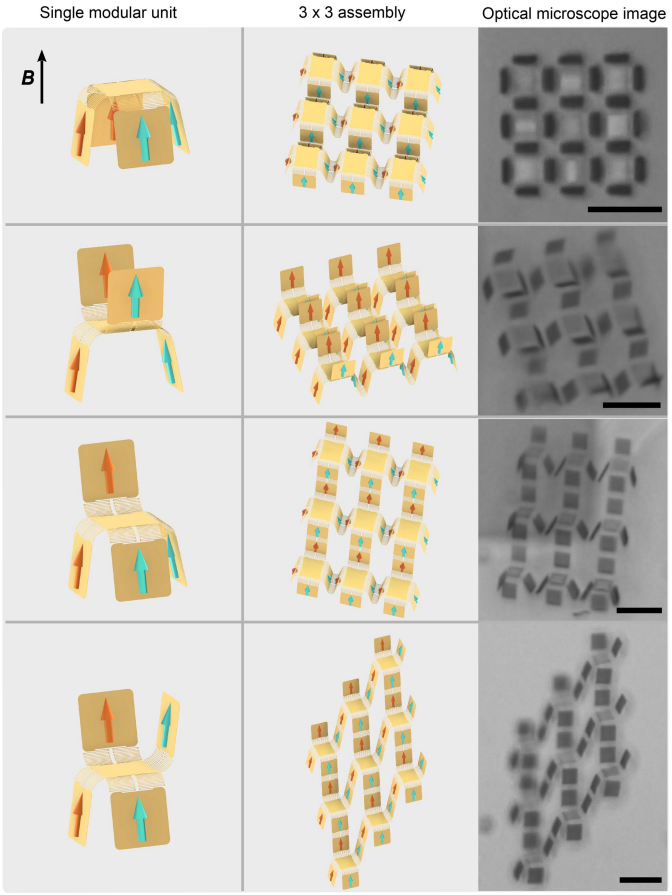


**Extended Data Fig. 5 | Four conformations of a micromachine consisting of a 3 × 3 assembly of four-panel modular units.** Shown in the middle and right panels are schematics and experimental demonstrations of the actuated micromachines. The units in a given micromachine all have the same conformation (left panel) corresponding to one of the 16 different magnetization configurations. Scale bars in the optical microscope images, 30 μm.

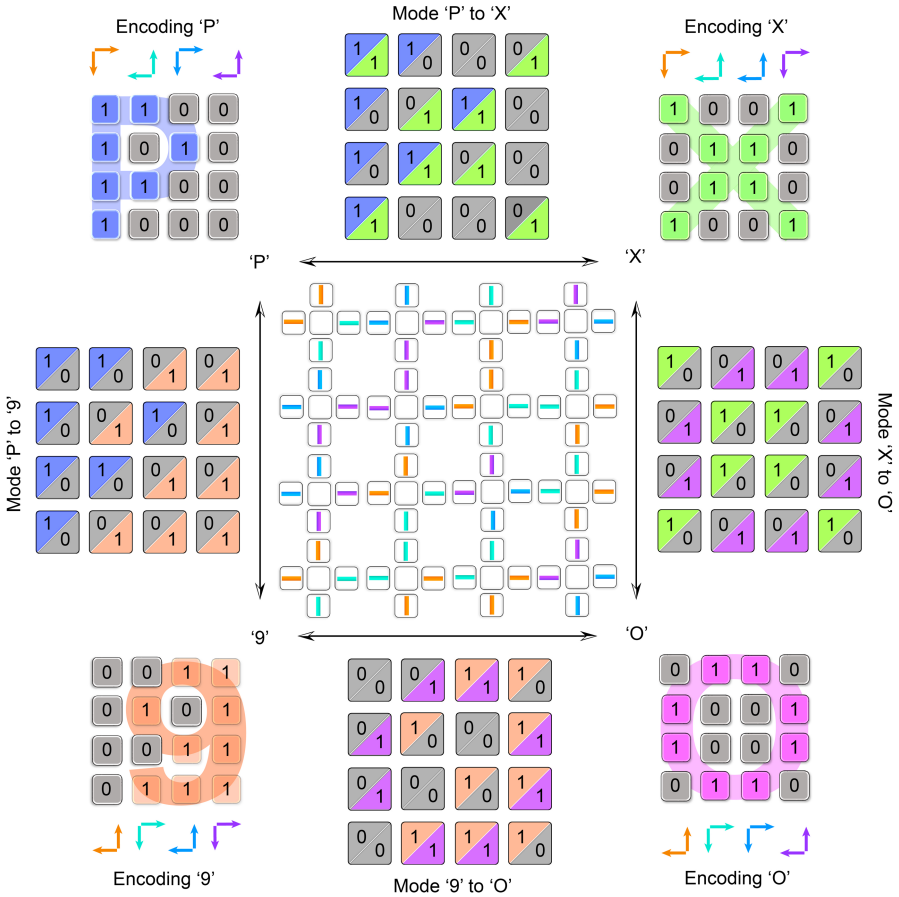


**Extended Data Fig. 6 | Four different modes, ‘P’, ‘X’, ‘O’ and ‘9’, encoded in the same micromachine design.** In the conjugate pairs (‘P’ and ‘9’, or ‘X’ and ‘O’), the ‘up’ and ‘down’ states of each unit are reversed. With a different nanomagnet encoding, a single micromachine with this design can transform between these four modes. See main text and Methods for details.

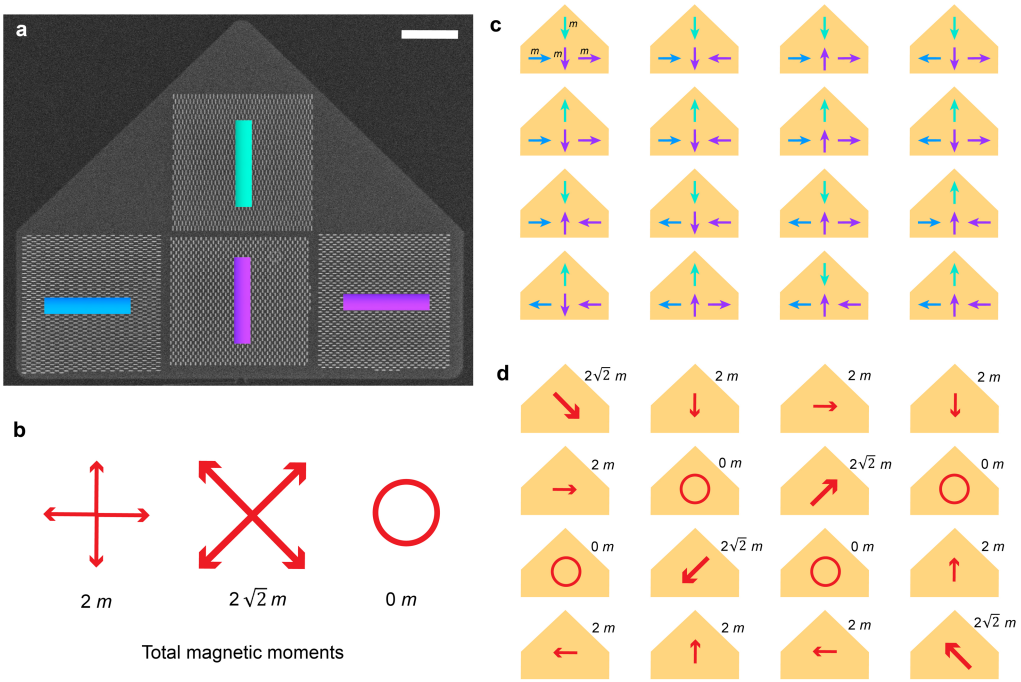


**Extended Data Fig. 7 | Possibilities for the total magnetic moments of the wing tip in the microscale 'bird'. a**, SEM image of the wing tip of the microscale bird. Turquoise vertical bar, type II nanomagnets (398 nm × 80 nm); blue horizontal bar, type III nanomagnets (358 nm × 90 nm); purple bar (horizontal and vertical), type IV nanomagnets (300 nm × 110 nm). Each of the arrays has the same number of magnets (1,040) with the same magnetic moment *m*. **b**, Nine possible total magnetic moment magnitudes and directions. **c**, Schematics of 16 possible magnetic configurations of the wing tip. Each of the arrays of different types of nanomagnets (types II, III and IV) have different switching fields, and there are two out of the four arrays that have the same type IV magnets but with orthogonal orientation. Therefore, with the orientation of the nanomagnets in two of the arrays along the *x* direction and in the two other arrays along the *y* direction, there are in total $2^2 \times 2^2 = 16$ possible magnetic configurations that can be encoded into the wing tip. **d**, Schematics showing the magnitudes and directions of the total magnetic moment of the wing tip, corresponding to the 16 magnetic configurations shown in **c**. Scale bar in **a**, 4 µm.

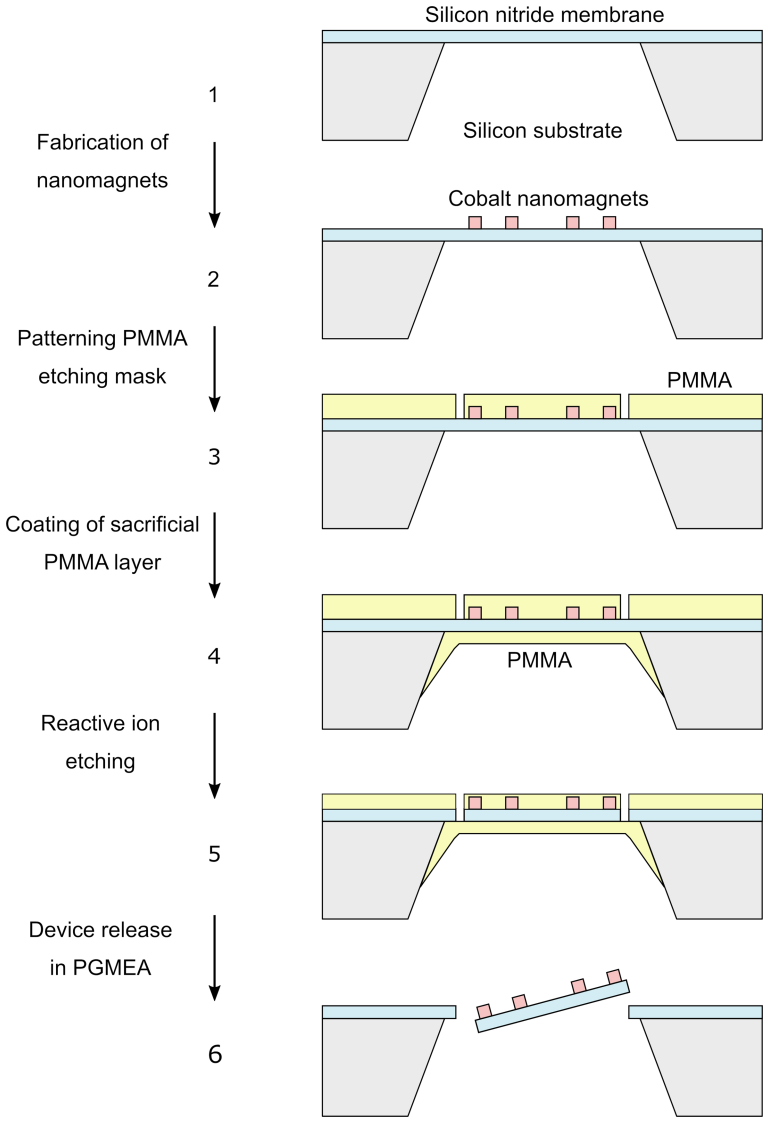


**Extended Data Fig. 8 | Schematic of the steps used to fabricate the micromachines.** The nanomagnets are fabricated using electron beam lithography, including patterning of a spin-coated polymer resist, thermal evaporation of a cobalt thin film and lift off. See Methods section 'Sample fabrication' for more details about the individual steps.

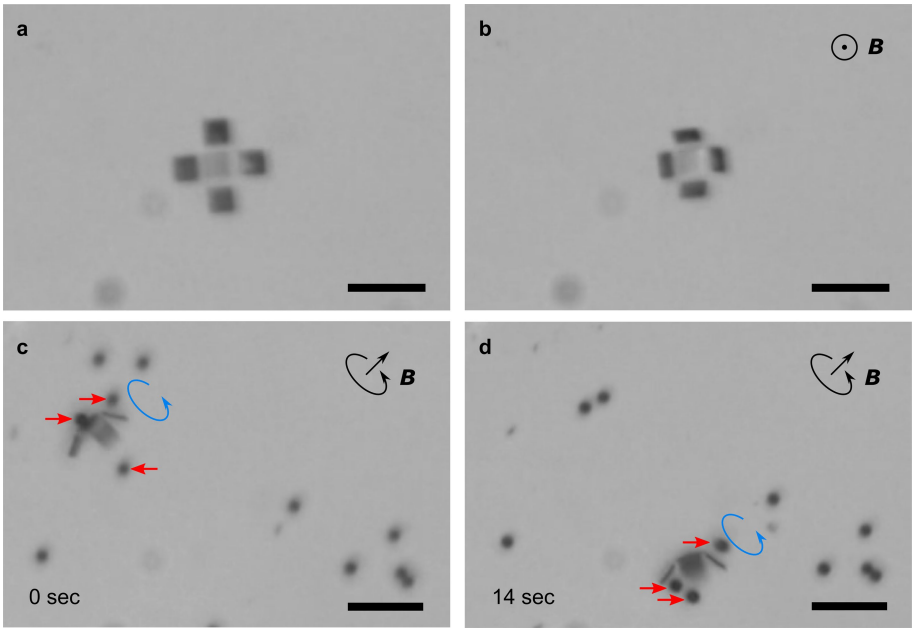


**Extended Data Fig. 9 | Optical microscope images of a four-panel micromachine, demonstrating operation in water and manipulation of polystyrene microbeads.** The micromachine is released in acetone and then a substitution of water for acetone is performed. The magnetization of all four panels points towards the centre. **a**, Micromachine in water without a magnetic field. **b**, The micromachine panels fold up in an applied out-of-plane magnetic field $\boldsymbol{B}$ of 10 mT. **c**, **d**, On application of a rotating magnetic field $\boldsymbol{B}$ (10 mT, 5 Hz), the micromachine rolls across the surface of a silicon wafer, and the rolling motion generates a vortex in the water surrounding it (highlighted with blue arrows). Polystyrene microbeads of 6 µm diameter (highlighted with red arrows) are trapped in the vortex and are transported to a new location. Two snapshots of the motion, separated by a time interval of 14 seconds, are shown. Scale bars, 40 µm.

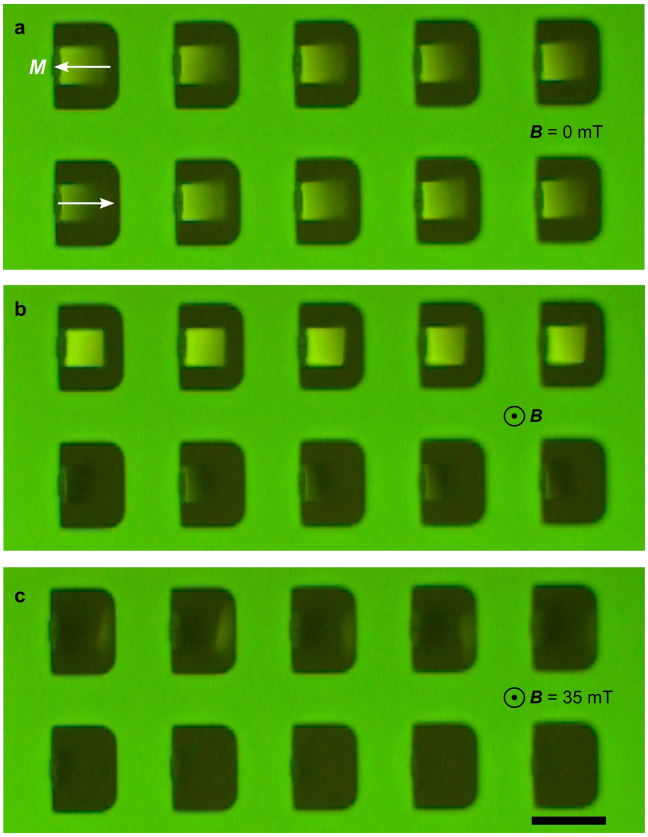


**Extended Data Fig. 10 | Optical microscope images of single-panel micromachines operating in air.** Two rows of single-panel micromachines are shown, each suspended within a D-shaped 'cutout' in the silicon nitride membrane frame, and connected to it on the left side by hinge springs with two turns. Each panel is 10 μm × 10 μm in size. **a**, After fabrication, the panels are somewhat out-of-focus. This is because they are slightly tilted above the plane of the in-focus silicon nitride frame, which may be due to the residual stress in the hinge springs. The white arrows indicate the magnetization direction of the single-panel micromachines pointing left (top row) and right (bottom row). **b**, **c**, On slowly increasing the applied out-of-plane magnetic field, the panels tilt downwards (top row) or upwards (bottom row), with the tilt angle increasing as the field magnitude is increased. In the optical images, the panels with magnetization pointing to the left (top row) first become sharper (**b**), and they almost disappear at a tilt angle close to 90° at 35 mT (**c**). The panels with magnetization direction pointing to the right (bottom row) tilt upwards in the applied magnetic field, becoming less visible as the field is increased (**b**), until finally disappearing when the tilt angle is close to 90° at 35 mT (**c**). Scale bar (for **a**–**c**), 20 μm.